Shear driven waves in the induced magnetosphere of Mars

H Gunell[1], U V Amerstorfer[2,3], H Nilsson[4], C Grima[5], M Koepke[1], M Fränz[6], J D Winningham[7], R A Frahm[7], J-A Sauvaud[8], A Fedorov[8], N V Erkaev[9], H K Biernat[2,3], M Holmström[4], R Lundin[4] and S Barabash[4]

[1] Department of Physics, West Virginia University, Morgantown, WV 26506-6315, USA
[2] Space Research Institute, Austrian Academy of Sciences, Schmiedlstr. 6, A-8042 Graz, Austria
[3] Institute of Physics, University of Graz, Universitätsplatz 5, A-8010 Graz, Austria
[4] Swedish Institute of Space Physics, P.O. Box 812, SE-981 28 Kiruna, Sweden
[5] Laboratoire de Planétologie de Grenoble, BP-53, F-38041 Grenoble Cedex 9, France
[6] Max-Planck-Institut für Sonnensystemforschung, Max-Planck-Straße 2, 37191 Katlenburg-Lindau, Germany
[7] Southwest Research Institute, San Antonio, TX 7228-0510, USA
[8] Centre d'Etude Spatiale des Rayonnements, BP-4346, F-31028 Toulouse, France
[9] Institute of Computational Modelling, Russian Academy of Sciences, 660036 Krasnoyarsk-36, Russia

E-mail: herbert.gunell@physics.org

Abstract

We present measurements of oscillations in the electron density, ion density and ion velocity in the induced magnetosphere of Mars. The fundamental frequency of the oscillations is a few millihertz, but higher harmonics are present in the spectrum. The oscillations are observed in a region where there is a velocity shear in the plasma flow. The fundamental frequency is in agreement with computational results from an ideal-MHD model. An interpretation based on velocity-shear instabilities is described.

1. Introduction

Recent electron measurements by the Mars Express [1] spacecraft and magnetic field measurements by the Mars Global Surveyor [2] have shown oscillations in Mars' magnetosheath, induced magnetosphere and tail. The frequency of the integrated electron energy flux is typically peaked between 0.01 and 0.02 Hz. The typical O^+ gyro-frequency in the magnetosheath, calculated using magnetometer data from Mars Global Surveyor, is in this range [2]. The observed amplitudes were highest near the bow shock (BS) nose and decreased further downstream [1].

At Venus, observations of wave-like structures in the plasma were made by the Pioneer Venus Orbiter. These structures were seen in the upper part of the dayside ionosphere.

Plasmoids of ionospheric plasma, separated from the ionosphere by a region of magnetosheath plasma, were observed near the terminator and further downstream [3, 4]. The observed separation was perpendicular to the plasma flow in the magnetosheath and this has been interpreted as an indication of a wave associated with an instability at the ionopause. Such instabilities have been studied in the framework of magnetohydrodynamics (MHD) [5, 6] and by the use of a two-dimensional global hybrid simulation [7]. These studies showed that a Kelvin–Helmholtz instability at the boundary layer can be the cause of the observed wave structures and the detachment of plasmoids from the ionosphere. Lammer *et al* [8] published predictions of escape rates for the different processes that are thought to be responsible for atmospheric escape from Venus. They found that 'the Kelvin–Helmholtz instability may be responsible for a loss rate of O^+ ions on Venus in the order of about 10^{25} s^{-1}'.

The Kelvin–Helmholtz instability [9, 10] is the lowest frequency example of velocity-shear-induced instabilities [11, 12]. Higher-frequency instabilities in this category cover ion-acoustic, ion-cyclotron and lower-hybrid frequencies. The higher-efficiency process of gyro-resonant ion-cyclotron heating [13] is attractive for explaining outflow of heavy ions of planetary origin.

The interaction between the solar wind and Mars has been studied using single-fluid MHD models [14], single-fluid, multi-species MHD models [15, 16], two-ion MHD models [17, 18] and hybrid models [19, 20].

In this paper, a case study based on measurements from one orbit of the Mars Express spacecraft is presented. We present measurements of simultaneous oscillations in both the electron and ion densities and in the ion velocity inside the induced magnetosphere at Mars. The observations, that were made using the Analyzer of Space Plasmas and Energetic Atoms (ASPERA-3) [21] on the Mars Express spacecraft, are compared to MHD computations of the Kelvin–Helmholtz instability. Nilsson *et al* [22] reported observations of a number of 'ion beam events' for the December 2005 to March 2006 period. These ion beams showed a fine structure that is consistent with the case that is studied in more detail here.

2. Mars express data

We analyse data from Mars Express orbit 2510 between 11:15 and 11:45 UT on 26 December 2005. The orbit is shown in figure 1. The Mars-centred Solar Orbital coordinate system is used in this paper. The x-axis is directed from the centre of Mars towards the sun, the z-axis is northward and perpendicular to Mars' orbital plane and the y-axis completes the right handed system. Figure 1(*a*) shows a projection of the orbit on the y–z plane. Figure 1(*b*) shows the orbit in a cylindrical coordinate system, where the vertical axis is the distance to the Mars–Sun line, i.e. $\rho = \sqrt{y^2 + z^2}$. Both axes are normalized to the radius of Mars. The BS and the IMB are shown as dashed lines. The measurements that are analysed in this paper were performed between 11:15 and 11:45 UT, and the positions of the spacecraft at these times are marked in the figures. Figure 1(*c*) shows the geometry of the calculations that are presented in section 3.

The IMB is the boundary which separates the solar wind from the inner region that is dominated by plasma of planetary origin. It has been given many different names in the literature depending on what measured quantity has been used to identify it. We call it the IMB following [23]. Whether the IMB is the same boundary as the magnetic pile-up boundary [24] cannot be determined by Mars Express that does not carry a magnetometer.

During the interval of interest here, the spacecraft was in the induced magnetosphere. Electron and ion energy spectra are shown in figure 2. Oxygen and carbon dioxide ions were observed by the ion mass analyzer (IMA). The IMA was operated in a mode where it, every 12 s, obtained spectra, in the 30 eV to 30 keV energy range, from 16 sectors that together cover
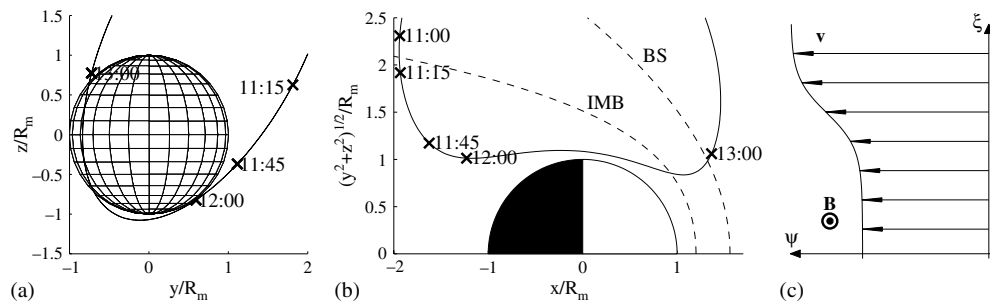
Figure 1. (*a*) Mars Express orbit 2510 on 26 December 2005, in the *y*–*z* plane, i.e. viewed from the direction of the sun. (*b*) The same orbit in a cylindrical coordinate system. The sun is in the positive *x*-direction. The vertical axis shows the distance to the *x*-axis normalized to the radius of Mars. The dashed lines show the bow shock (BS) and the induced magnetosphere boundary (IMB). (*c*) Geometry of the MHD calculations described in section 3.
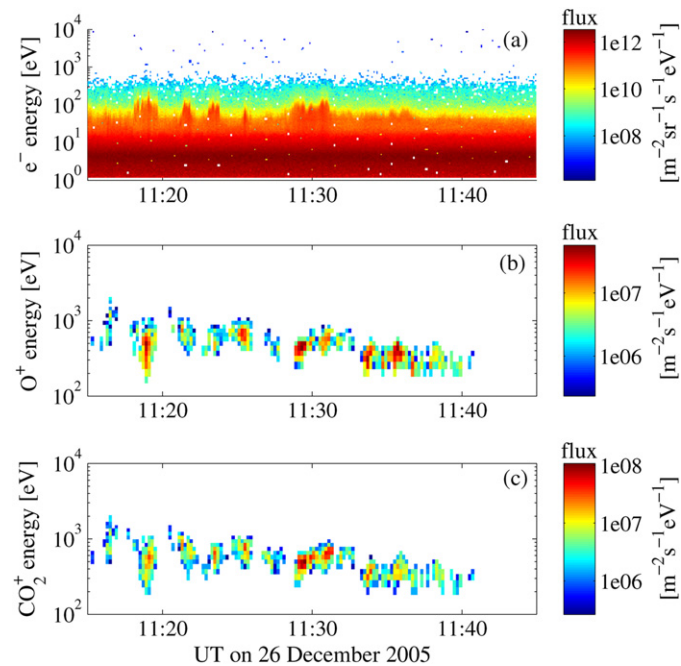

Figure 2. (*a*) Electron energy spectra versus time for the period from 11:15 until 11:45 UT on 26 December 2005, (*b*) O^+-ion spectra for the same period and (*c*) CO_2^+-ion spectra. Integrals over the vertical direction in the figures are proportional to the particle density. Peaks in the particle flux occur simultaneously in all three panels.

(This figure is in colour only in the electronic version)

360° in one plane. Ion mass resolution is achieved by deflection of particles in a magnetic field set up by permanent magnets. The instrument is thus able to distinguish between oxygen and carbon dioxide ions. In figures 2(*b*) and (*c*), the sum of the 16 sectors is shown, but the dominating signal came from only one sector. The observed ions arrive at the spacecraft from the direction of a region near the equatorial terminator.
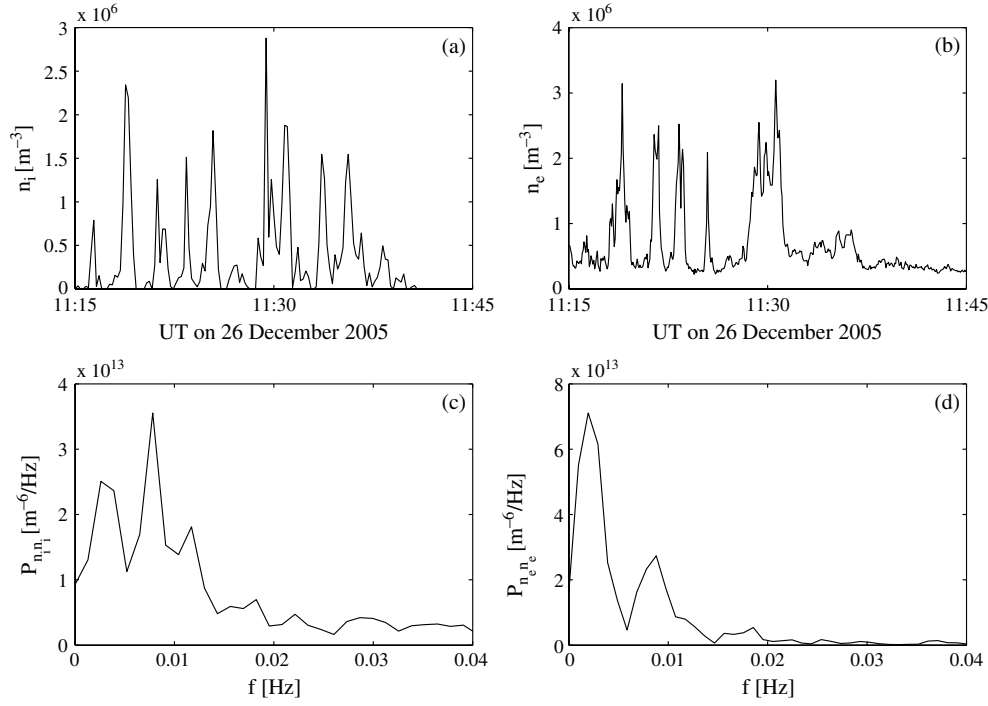
Figure 3. (*a*) Ion density from a sum of figures 2(*b*) and (*c*); (*b*) electron density from figure 2(*a*); (*c*) power spectral density of the ion density, i.e. figures (*a*); and (*d*) power spectral density of the electron density, i.e. figure (*b*).

The electron spectra were measured using the electron spectrometer (ELS) and are shown in figure 2(*a*). Every 4 s, spectra were obtained from 16 sectors that together cover 360° in one plane. Figure 2(*a*) shows the average of the spectra from the 16 sectors. The spectra obtained by the sixteen different sectors are similar, as is expected from an isotropic electron velocity distribution. Below 20 eV, the electron spectra are dominated by photo-electrons emitted from the spacecraft. The ambient plasma has an electron temperature, $k_B T_e \approx 40$ eV.

Figure 3(*a*) shows the ion density, $n_i = n_{O^+} + n_{CO_2^+}$. Each IMA sector covers a $22.5° \times 4.5°$ field of view. The observed ion beam is about one sector wide, i.e. 22.5°, in the plane where all sectors are located. The density has been calculated assuming that the width is 22.5°, also in the direction perpendicular to this plane, where only the 4.5° opening angle is sampled. The lower energy limit of the IMA is 30 eV and therefore n_i should be seen as the contribution to the ion density from ions with energies above 30 eV. The electron density n_e is shown in figure 3(*b*). The average of the particle flux collected by the different sectors was used to calculate n_e. An isotropic velocity distribution was assumed. To avoid the contribution from photo-electrons emitted by the spacecraft, only electrons with energies above 30 eV were included.

There are oscillations in both the electron and ion densities. These are also evident in the spectra in figure 2. Figure 3(*c*) shows the power spectral density $P_{n_i n_i}$ of $n_i - \langle n_i \rangle$, where $\langle n_i \rangle$ is mean value of the density during the time shown in figure 3(*a*). Similarly, figure 3(*d*) shows the power spectral density $P_{n_e n_e}$ of $n_e - \langle n_e \rangle$. The power spectral density was computed using Welch's method, described in [25], with a Hanning window and 65% overlap. The ion and electron density time series agree well between 11:18 and 11:31. The power spectral density
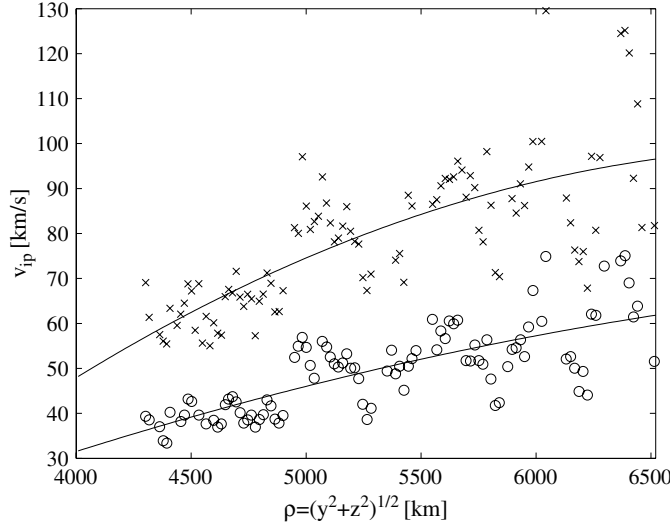
Figure 4. Ion speeds in the plane of figure 1 for oxygen ions ($\times$) and carbon dioxide ions ($\bigcirc$). The solid curves show polynomial fits to the data, $v_{ip} = c_0 + c_1\rho + c_2\rho^2$, where $c_0 = -1.55 \times 10^5$ m s^{-1}, $c_1 = 0.0701$ s^{-1} and $c_2 = -4.83 \times 10^{-9}$ m^{-1} s^{-1} for O$^+$ and $c_0 = -5.88 \times 10^4$ m s^{-1}, $c_1 = 0.029$ s^{-1} and $c_2 = -1.62 \times 10^{-9}$ m^{-1} s^{-1} for CO$_2^+$.

peaks at $2\,\text{mHz} \leqslant f \leqslant 3\,\text{mHz}$ and $8\,\text{mHz} \leqslant f \leqslant 9\,\text{mHz}$. The sampling frequencies are different in figures 3(*c*) and (*d*), specifically, $\frac{1}{4}$ Hz for the electrons and $\frac{1}{12}$ Hz for the ions, and therefore the peaks do not overlap exactly. A third peak at $11\,\text{mHz} \leqslant f \leqslant 12\,\text{mHz}$ is evident in the ion spectrum.

The ion velocity can be derived from the IMA data. In the cylindrical coordinate system in figure 1(*b*), the azimuthal component of the velocity is negligible, i.e. the velocity vector is in the plane of figure 1(*b*). Figure 4 shows the in-plane component of the ion velocity for O$^+$ and CO$_2^+$ ions as a function of the cylindrical coordinate ρ. The lighter O$^+$ ions are faster than the CO$_2^+$ ions by a factor that is close to the square root of the mass ratio, showing that the two ion species have approximately the same energy. There is a velocity shear in the ion flow with faster ions at higher values of ρ. Polynomials, $v_{ip} = c_0 + c_1\rho + c_2\rho^2$, fit to the data are shown as solid lines in figure 4. For oxygen, $c_0 = -1.55 \times 10^5$ m s^{-1}, $c_1 = 0.0701$ s^{-1} and $c_2 = -4.83 \times 10^{-9}$ m^{-1} s^{-1} and, for carbon dioxide, $c_0 = -5.88 \times 10^4$ m s^{-1}, $c_1 = 0.029$ s^{-1} and $c_2 = -1.62 \times 10^{-9}$ m^{-1} s^{-1}.

The magnitude of the velocity oscillates around its equilibrium value given by the polynomial fit. The oscillating components $\tilde{v}_{\text{O}^+}$ and $\tilde{v}_{\text{CO}_2^+}$ of the O$^+$ and CO$_2^+$ velocities are shown in figures 5(*a*) and (*b*) as functions of time. The oscillating component is found by subtracting the polynomial fit from the data so that $\tilde{v}_{\text{O}^+} = v_{\text{O}^+} - (c_0 + c_1\rho + c_2\rho^2)$ for O$^+$ and analogously for CO$_2^+$. Figure 5(*c*) shows the power spectral density of $\tilde{v}_{\text{O}^+}$ and figure 5(*d*) shows the power spectral density of $\tilde{v}_{\text{CO}_2^+}$. The frequency of the velocity oscillations coincides with the fundamental frequency of the density oscillations.

The most easily distinguishable peaks in the times series in figure 3 correspond to the peak at $8\,\text{mHz} \leqslant f \leqslant 9\,\text{mHz}$ in the power spectrum, whereas the fundamental frequency is seen as a modulation of these peaks in the ion times series. The fundamental frequency is seen most clearly in the velocity data (figure 5), and can be seen in the energy spectrograms as well. It is not so easy to see in the time series of the electron data, but it is revealed in the power spectral density in figure 3(*d*).
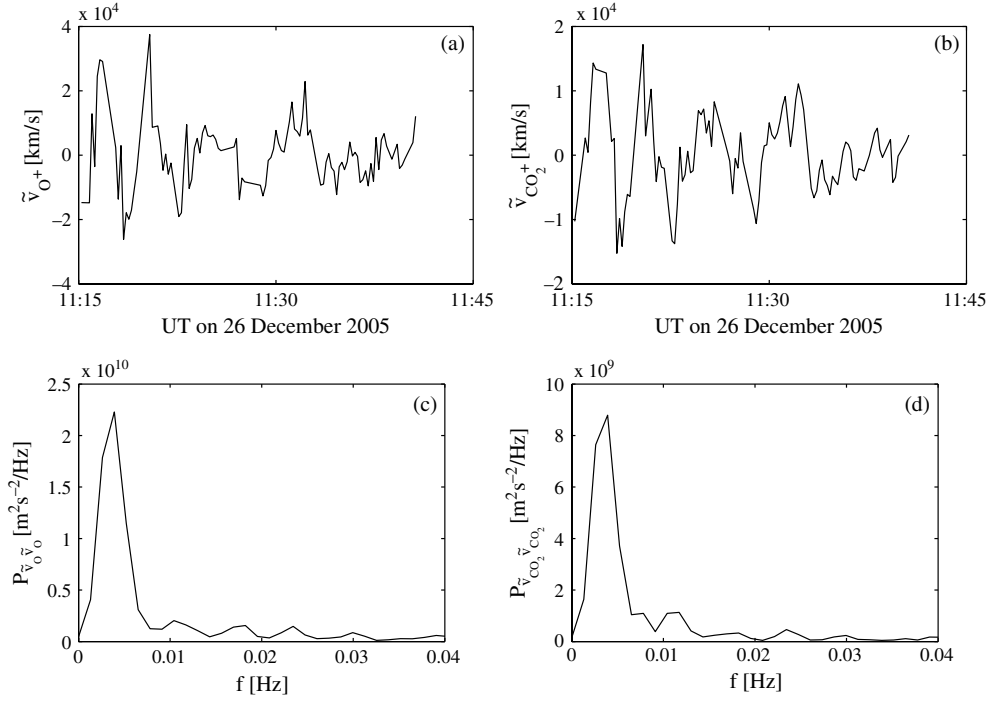
Figure 5. The oscillating part of the ion velocity magnitude for O^+ (*a*) and CO_2^+ (*b*) and power spectral density of the oscillating part of the velocity for O^+ (*c*) and CO_2^+ (*d*). For both, the peak is located at $3\,\text{mHz} \leqslant f \leqslant 4\,\text{mHz}$.

3. Computations

We model the sheared flow using a one-dimensional ideal MHD model with two ion species [26]. The linearized MHD equations have been solved for six cases with different parameters, and growth rates and wave numbers have been calculated in each case. The model uses two separate continuity equations for O^+ and CO_2^+, three different adiabatic relations for O^+, CO_2^+ and electrons, but only one momentum equation. Thus the different species have the same bulk velocity in the model, but can have different densities and temperatures. The measurements show that the ions have equal energies rather than equal velocities. We explore the effect of the velocity dependence by calculating three cases with only O^+ ions, using a velocity profile that is estimated from the O^+ measurements, and three cases with both O^+ and CO_2^+, using a velocity profile that is a weighted average of the measured velocities of O^+ and CO_2^+.

The model coordinate system (ξ, ψ, ζ) is shown in figure 1(*c*). In the following, $\hat{\boldsymbol{\xi}}$, $\hat{\boldsymbol{\psi}}$ and $\hat{\boldsymbol{\zeta}}$ denote unit vectors in the ξ-, ψ- and ζ-directions, respectively. The plasma flows in the ψ-direction. The magnetic field, $\boldsymbol{B}_0 = B_0\hat{\boldsymbol{\zeta}}$, is parallel to the ζ-axis. All equilibrium quantities are constants except the plasma velocity that depends on ξ. A smooth velocity-profile function is fitted to the measured data for each ion species. This fitted profile is given by

$$\boldsymbol{v}_0(\xi) = \left(a_1 \tanh\left(a_2 \frac{\xi}{\Delta\xi} \right) + a_3 \right) v_\text{m}\hat{\boldsymbol{\psi}}, \tag{1}$$

where $a_1 = 0.18$, $a_2 = 2.6$ and $a_3 = 0.82$. For large ξ, v_0 tends to the asymptotic limit v_m. Here $\Delta\xi = 2524\,\text{km}$ is the width of the shear layer. The parameters of the six different cases

Table 1. Parameters of the different cases, the maximum growth rate and the frequency of maximum growth. In all cases, $B_0 = 30$ nT, $k_B T_e = 40$ eV and $k_B T_i = 30$ eV.

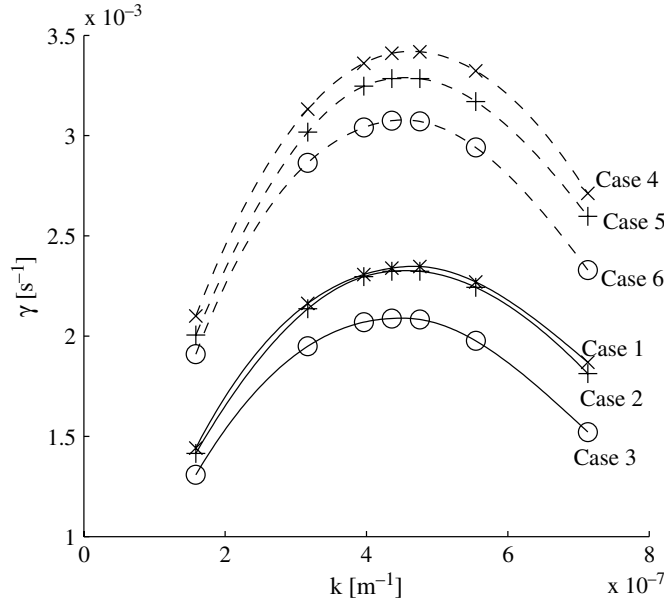| Case	n_{O^+} (cm^{-3})	$n_{CO_2^+}$ (cm^{-3})	n_e (cm^{-3})	v_m (km s^{-1})	f_m (mHz)	γ_m (s^{-1})
1	0.17	0.33	0.5	67.4	4.1	0.0023
2	1	2	3	67.4	4.0	0.0023
3	5.33	10.67	16	67.4	3.9	0.0021
4	0.5	0	0.5	96.4	5.8	0.0034
5	3	0	3	96.4	5.8	0.0033
6	16	0	16	96.4	5.7	0.0031

Figure 6. Kelvin–Helmholtz growth rates as functions of wave number for the six different cases in table 1. The parameters are shown in table 1. The symbols denote the calculated values of the growth rate, the lines show an interpolation between these points.

are shown in table 1, together with the maximum growth rate and the frequency for maximum growth. In the first three cases, two thirds of the ions are CO_2^+ and one third O^+. In cases 4–6, we consider a single ion species, namely O^+. In all cases, $B_0 = 30$ nT, $k_B T_e = 40$ eV and $k_B T_i = 30$ eV. In the case of an oxygen plasma, v_m is given directly by the fit to the O^+ data. For the case with both oxygen and carbon dioxide, a weighted average is used,

$$v_m = \frac{n_{O^+} m_{O^+} v_{m,O^+} + n_{CO_2^+} m_{CO_2^+} v_{m,CO_2^+}}{n_{O^+} m_{O^+} + n_{CO_2^+} m_{CO_2^+}}. \tag{2}$$

In all six cases, the plasma is Kelvin–Helmholtz unstable. The growth rates as functions of wave number are shown in figure 6. The Kelvin–Helmholtz instability creates a waveform that is stationary in the plasma rest frame. An observer that is stationary in the planetary frame will see a frequency that is Doppler-shifted by the ion flow speed. Assuming an ion flow speed

corresponding to $\xi = 0$ in (1), the frequency values shown in table 1 are given by

$$f = a_3 v_m \frac{k}{2\pi}. \tag{3}$$

The variation in the wave number of maximum growth between the different cases is small. The frequency is about 4 mHz in the two-ion plasma and about 6 mHz in the O^+-ion plasma. In section 2, a fundamental frequency of 2–3 mHz was observed in the measurements. The growth rates are higher in the single-ion cases (4–6), with their larger velocity shear, than in the two-ion cases (1–3), where the velocity shear is smaller. Within each group (1–3 and 4–6), the growth rate decreases with increasing density.

4. Conclusions and discussion

Oscillations in density and velocity are observed at a fundamental frequency of about 2–3 mHz in the induced magnetosphere of Mars. We have calculated frequencies and growth rates for the Kelvin–Helmholtz instability using a linearized one-dimensional MHD-model with a velocity profile that is estimated from the satellite measurements. Of the six calculated cases, cases 1 and 2 are those that best resemble the measured data, having two ion species and low values of density. Both of these cases yield frequencies around 4 mHz and growth rates of $0.0023\,\mathrm{s}^{-1}$. The agreement is reasonable for the frequencies. At the observed ion velocities, it takes the plasma about 100 s to travel from the planet out to the region where the observations were made. With this calculated growth rate, the growth factor corresponds to $\mathrm{e}^{0.23} \approx 1.26$, i.e. approximately 26% growth.

The plasma at the location of the observations was unstable to the Kelvin–Helmholtz instability. While the frequency is in reasonable agreement with observations, the growth rate is not high enough to explain the large amplitudes and the presence of higher harmonics. Thus the simplified physics of a one-dimensional linear model can only partially explain the observations. The growth rate could possibly be higher close to the planet due to a larger velocity shear in that region. The wave could thus have grown more than our calculation indicates before it reached the spacecraft. However, if the value of the velocity shear is higher, not only the growth rate but also the frequency would increase, and therefore, while this hypothesis would give a larger amplitude, it is not consistent with the frequency match between model and measurements. The assumption that all ion species have the same bulk velocity is a potential weakness of the model. However, the calculations of the cases with only oxygen ions and their higher speeds did give higher growth rates, but the highest growth rate was still not more than $0.0034\,\mathrm{s}^{-1}$ in case 4.

If the Kelvin–Helmholtz instability develops into a non-linear state where the vortices form, this would be seen as higher harmonics by a stationary observer. Also, the growth of the Kelvin–Helmholtz instability can lead to the formation of localized gradients and the development of microinstabilities [27].

References

[1] Winningham J D *et al* 2006 Electron oscillations in the induced martian magnetosphere *Icarus* **182** 360–70

[2] Espley J R, Cloutier P A, Brain D A, Crider D H and Acuña M H 2004 Observations of low-frequency magnetic oscillations in the Martian magnetosheath, magnetic pileup region, and tail *J. Geophys. Res.* **109** A07213

[3] Brace L H, Theis R F and Hoegy W R 1982 Plasma clouds above the ionopause of Venus and their implications *Planet. Space Sci.* **30** 29–37

[4] Russell C T, Luhmann J G, Elphic R C, Scarf F L and Brace L H 1982 Magnetic field and plasma wave observations in a plasma cloud at Venus *Geophys. Res. Lett.* **9** 45–8

[5] Wolff R S, Goldstein B E and Yeates C M 1980 The onset and development of Kelvin–Helmholtz instability at the Venus ionopause *J. Geophys. Res.* **85** 7697–707

[6] Elphic R C and Ershkovich A I 1984 On the stability of the ionopause of Venus *J. Geophys. Res.* **89** 997–1002

[7] Terada N, Machida S and Shinagawa H 2002 Global hybrid simulation of the Kelvin–Helmholtz instability at the Venus ionopause *J. Geophys. Res.* **107** 1471

[8] Lammer H *et al* 2006 Loss of hydrogen and oxygen from the upper atmosphere of Venus *Planet. Space Sci.* **54** 1445–56

[9] Chandrasekar S 1961 *Hydrodynamic and Hydromagnetic Stability* (Oxford: Clarendon) chapter 11

[10] Kent G I, Jen N C and Chen F F 1969 Transverse Kelvin–Helmholtz instability in a rotating plasma *Phys. Fluids* **12** 2140–51

[11] Gavrishchaka V, Koepke M E and Ganguli G 1996 Dispersive properties of a magnetized plasma with a field-aligned drift and inhomogeneous transverse flow *Phys. Plasmas* **3** 3091–106

[12] Lakhina G S 1987 Low-frequency electrostatic noise due to velocity shear instabilities in the regions of magnetospheric flow boundaries *J. Geophys. Res.* **92** 12161–70

[13] Rynn N, Dakin D R, Correll D L and Benford G 1974 Ion heating by the current-driven electrostatic ion-cyclotron instability *Phys. Rev. Lett.* **33** 765–8

[14] Shinagawa H and Bougher S W 1999 A two-dimensional MHD model of the solar wind interaction with Mars *Earth Planets Space* **51** 55–60

[15] Liu Y, Nagy A F, Groth C P T, DeZeeuw D L, Gombosi T I and Powell K G 1999 3D multi-fluid MHD studies of the solar wind interaction with Mars *Geophys. Res. Lett.* **26** 2689–92

[16] Ma Y, Nagy A F, Hansen K C, DeZeeuw D L and Gombosi T I 2002 Three-dimensional multispecies MHD studies of the solar wind interaction with Mars in the presence of crustal fields *J. Geophys. Res.* **107** 1282 doi:10.1029/2002JA009293

[17] Sauer K, Bogdanov A and Baumgärtel K 1994 Evidence of an ion composition boundary (protonopause) in bi-ion fluid simulations of solar wind mass loading *Geophys. Res. Lett.* **21** 2255–8

[18] Sauer K, Dubinin E and Baumgärtel K 1998 Nonlinear MHD waves and discontinuities in the Martian magnetosheath. Observations and 2D bi-ion MHD simulations *Earth Planets Space* **50** 793–801

[19] Brecht S H 1997 Solar wind proton deposition into the Martian atmosphere *J. Geophys. Res.* **102** 11287–94

[20] Kallio E and Janhunen P 2001 Atmospheric effects of proton precipitation in the Martian atmosphere and its connection to the Mars–solar wind interaction *J. Geophys. Res.* **106** 5617–34

[21] Barabash S *et al* 2006 The Analyzer of Space Plasmas and Energetic Atoms (ASPERA-3) for the Mars Express Mission *Space Sci. Rev.* **126** 113–64

[22] Nilsson H *et al* 2006 Investigation of the influence of magnetic anomalies on ion distributions at Mars *Space Sci. Rev.* **126** 355–72

[23] Lundin R *et al* 2004 Solar wind-induced atmospheric erosion at Mars: First results from ASPERA-3 on Mars express *Science* **305** 1933–6

[24] Vignes D, Mazelle C, Rème H, Acuña M H, Connerney J E P, Lin R P, Mitchell D L, Cloutier P, Crider D H and Ness N F 2000 The solar wind interaction with Mars: locations and shapes of the bow shock and the magnetic pile-up boundary from the observations of the MAG/ER experiment onboard Mars Global Surveyor *Geophys. Res. Lett.* **27** 49–52

[25] Stoica P and Moses R L 1997 *Introduction to Spectral Analysis* (Upper Saddle River, NJ: Prentice-Hall)

[26] Amerstorfer U V, Erkaev N V, Langmayr D and Biernat H K 2007 On Kelvin–Helmholtz instability due to the solar wind interaction with unmagnetized planets *Planet. Space Sci.* **55** 1811–6

[27] Ganguli G, Keskinen M J, Romero H, Heelis R, Moore T and Pollock C 1994 Coupling of microprocesses and macroprocesses due to velocity shear: an application to the low-altitude ionosphere *J. Geophys. Res.* **99** 8873–89